Investigation of Submerged Soil Excavation by High-Velocity Water Jet Using Two-Fluid Smoothed Particle Hydrodynamics Method

Qingqing Yuan, Ph.D.[1]; Chun Wang[2]; Yongqi Wang[3]; Chong Peng[4]; and Xiannan Meng, Ph.D.[5]

Abstract: In this paper, submerged soil excavation by high-velocity water jet was investigated by means of a two-fluid smoothed-particle hydrodynamics (SPH) method. A critical state theory was coupled to account for the dilatancy or compaction of the soil subjected to deformation. Numerical simulations for excavations by plane wall jet and vertical impinging jet are presented. The development of the crater size during the jetting process was obtained and found to be qualitatively in agreement with experimental observations and numerical simulations provided by other researchers. The effects of the nozzle width, impinging height, jetting velocity, and water flux on the formation of different crater patterns were examined. The effects of soil parameters, such as cohesion [in the range of $(0, 25$ kPa$)$] and dilatancy, were also investigated. Computational results illustrate the critical role of dilatancy in the coupling evolution of the solid volume fraction and pore fluid pressure by modifying the Coulomb friction and thereby regulating the dynamics of soil deformation. The proposed method is robust and efficient, and can be applied to water-soil mixture flows in subsea engineering and geomechanics. **DOI: 10.1061/(ASCE)HY.1943-7900.0001599.** © *2019 American Society of Civil Engineers.*

Author keywords: Submerged water jet soil excavation; Two-phase mixture model; Smoothed particle hydrodynamics (SPH) method; Numerical simulation.

Introduction

Submerged water jet soil excavation is a typical water-soil interaction problem that occurs widely in many engineering disciplines. In hydraulic engineering, it is a model of scour downstream of headcuts, culverts, or dam spillways. In port and waterway engineering, harbor and channel dredging and the erosion of the channel bed or quay wall by the propellers of passing ships are also typical water jet soil interaction problems. In ocean engineering, trenching by impinging high-velocity (normally larger than 10 m/s) water jet has been considered as an efficient method for cable and pipeline burial operation in order to protect them from being damaged by fishing or repetitive wave pounding. Due to its vast applications in different engineering disciplines, submerged water jet soil excavation has long been a research concern for geophysicists, hydrologists, and underwater engineers.

Notable works on jet scour include Aderibigbe and Rajaratnam (1996), Hogg et al. (1997), Ade and Rajaratnam (1998), Mazurek et al. (2001, 2003), Mazurek and Rajaratnam (2005), Mazurek and Hossain (2007), Rajaratnam and Mazurek (2003), Ansari et al. (2003), and Hill and Younkin (2006), to name a few. They concerned both the effects of the nozzle configuration (i.e., planar or circular, vertical or horizontal) and the soil type (i.e., cohesive or noncohesive, loose or dense) on the temporal evolution of the scour hole and its equilibrium profile. Perng and Capart (2008) studied the traveling plane jet erosion of noncohesive soil in a tank by experimental measurements and theoretical analysis. Yeh et al. (2009) also tested the performance of traveling jets in sand beds. The scour profile was found to be self-similar when normalized by appropriate-length scales. Machin et al. (2001), Hettinger and Machin (2005), and Machin and Allan (2011) conducted experimental studies to develop an engineering model for jet trenching in stiff clay. A soil-bearing capacity theory was proposed for the trench depth prediction. Zhang et al. (2016, 2017) also conducted experimental studies of jet trenching in stiff clay and proposed empirical formulas to predict the performance of jet trenching.

There are some works on numerical simulation of water-soil interaction problems based on two-fluid smoothed-particle hydrodynamics (SPH) approaches. Manenti et al. (2012) applied an SPH-based numerical model to analyze the coupled fluid-sediment dynamics induced by the rapid water discharge in an artificial reservoir. Ulrich et al. (2013) studied the harbor bed erosion induced by the starting propeller of a large full-scale container vessel. Amicarelli et al. (2013, 2017) developed an SPH model based on the mixture model. The model was validated on the results from several experiments on erosional dam breaks. Wang et al. (2016b, 2018) proposed an incompressible smoothed-particle hydrodynamics (ISPH) method to simulate the scouring processes under different conditions. Concepts of numerical turbidity water particle and

[1]Ph.D. Candidate, Collaborative Innovation Center for Advanced Ship and Deep-Sea Exploration, School of Naval Architecture, Ocean and Civil Engineering, Shanghai Jiao Tong Univ., 800 Dongchuan Rd., Shanghai 200240, PR China.

[2]Associate Professor, Collaborative Innovation Center for Advanced Ship and Deep-Sea Exploration, School of Naval Architecture, Ocean and Civil Engineering, Shanghai Jiao Tong Univ., 800 Dongchuan Rd., Shanghai 200240, PR China (corresponding author). Email: chunwang@sjtu.edu.cn

[3]Professor, Chair of Fluid Dynamics, Dept. of Mechanical Engineering, Technische Universität Darmstadt, Otto-Berndt-Str. 2, Darmstadt 64287, Germany.

[4]Postdoctoral Researcher, Institute of Geotechnical Engineering, Universitaet fuer Bodenkultur, Feistmantelstrasse 4, Vienna 1180, Austria.

[5]Research Fellow, Centre for Offshore Research and Engineering, National Univ. of Singapore, 1 Engineering Dr. 2, Singapore 117576.

Note. This manuscript was submitted on January 9, 2018; approved on November 5, 2018; published online on March 20, 2019. Discussion period open until August 20, 2019; separate discussions must be submitted for individual papers. This paper is part of the ***Journal of Hydraulic Engineering***, © ASCE, ISSN 0733-9429.

incipient motion were proposed to deal with the sediment entrainment and erosion.

Recently, a two-fluid SPH mixture model to analyze the water jet soil interaction problem was proposed by Wang et al. (2016a). Key factors influencing the jet performance, namely, the internal friction angle and the hydraulic conductivity of the soil, were investigated, which helps reveal the mechanisms of soil failure under the impingement of a water jet. However, in this paper, the effects of ambient water on the excavation operation were not taken into consideration. In practical engineering, the operation environment is often underwater, so it is very important to consider the effects of the surrounding water on the excavation. More recently, in Wang et al. (2017a, b), a dilatancy coupled SPH model was developed to describe the effects of the ambient fluid on the granular flow.

In this paper, the proposed two-fluid SPH mixture model was employed to analyze the problem of submerged water jet soil excavation. The effects of nozzle diameter, jet velocity, height of the nozzle exit above the soil surface, water flux, and soil cohesion on the excavation were investigated, which helps reveal the characteristics of water jet soil excavation. Computational results also illustrate the critical role of dilatancy or compaction in linking coevolution of the solid volume fraction and pore fluid pressure during the process of submerged water jet soil excavation. Thus they should be considered in practical excavation engineering.

Mathematical Formulation

Water-Soil Mixture Model

In two-phase mixture theory (Bear and Buchlin 1991; Jackson 2000), each phase must satisfy individual balance laws for the conservation of mass

$$\frac{d^{\eta}\rho_{\eta}}{dt} = -\rho_{\eta}\nabla\cdot\mathbf{v}_{\eta} \tag{1}$$

and momentum

$$\rho_{\eta}\frac{d^{\eta}\mathbf{v}_{\eta}}{dt} = \nabla\cdot\boldsymbol{\sigma}_{\eta} + \rho_{\eta}\mathbf{g} + \mathbf{f}_{\eta} \tag{2}$$

where $d^{\eta}(\cdot)/dt$ = material time derivative along the path of particles of η phase ($\eta = l, s$ stands for fluid and solid, respectively); $\mathbf{g}$ = gravitational acceleration; and $\mathbf{f}_{\eta}$ = interaction force exerted on phase η by the other phase ($\mathbf{f}_l + \mathbf{f}_s = \mathbf{0}$). Here, partial density ρ_{η}, partial velocity $\mathbf{v}_{\eta}$, and partial stress $\boldsymbol{\sigma}_{\eta}(\eta = l, s)$ for each phase are defined as

$$\rho_{\eta} = \phi_{\eta}\tilde{\rho}_{\eta}, \qquad \mathbf{v}_{\eta} = \tilde{\mathbf{v}}_{\eta}, \qquad \boldsymbol{\sigma}_s = \phi_s\tilde{\boldsymbol{\sigma}}_s, \qquad \boldsymbol{\sigma}_l = -pI + \phi_l\tilde{\boldsymbol{\tau}}_l \tag{3}$$

where $\tilde{\rho}_{\eta}$ = intrinsic or true density of phase η; $\tilde{\mathbf{v}}$ = intrinsic velocity; $\tilde{\boldsymbol{\sigma}}_s$ = intrinsic stress of the soil; p = pore water pressure; $\tilde{\boldsymbol{\tau}}_l$ = intrinsic deviatoric stress tensor of water; and ϕ_{η} = volume fraction of phase η, satisfying $\phi_l + \phi_s = 1$ for a saturated liquid-solid mixture. The interaction force $\mathbf{f}_s$ (i.e., $-\mathbf{f}_l$) is assumed to take the form

$$\mathbf{f}_s = -\phi_s\nabla p + C_d(\mathbf{v}_l - \mathbf{v}_s) \tag{4}$$

where the first term on the right-hand side is a buoyancy force, and the second term is an interphase resistance term, with C_d being the drag coefficient. The value of C_d can be calculated according to Darcy's law (Wang et al. 2017b). With this in mind, the momentum equations are rewritten as

$$\rho_l\frac{d^l\mathbf{v}_l}{dt} = -\phi_l\nabla p + \nabla\cdot(\phi_l\tilde{\boldsymbol{\tau}}_l) + \rho_l\mathbf{g} - C_d(\mathbf{v}_l - \mathbf{v}_s) \tag{5}$$

$$\rho_s\frac{d^s\mathbf{v}_s}{dt} = -\phi_s\nabla p + \nabla\cdot(\phi_s\tilde{\boldsymbol{\sigma}}_s) + \rho_s\mathbf{g} + C_d(\mathbf{v}_l - \mathbf{v}_s) \tag{6}$$

Furthermore, a critical state theory (Pailha and Pouliquen 2009) is employed to take the dilatancy effect into account. According to this theory, the relation between the dilatancy angle ψ and the soil volume fraction ϕ_s is given by Pailha et al. (2008)

$$\frac{1}{\phi_s}\frac{d\phi_s}{dt} = -\tan\psi|\dot{\gamma}| \tag{7}$$

$$\tan\psi = K_3(\phi_s - \phi_{eq}) \tag{8}$$

where ϕ_{eq} = granular volume fraction obtained in the steady regime; K_3 = constant; $\dot{\gamma}$ = shear rate tensor ($\dot{\gamma}_{ij} = (1/2)(v_{i,j} + v_{j,i}) - (1/3)v_{\alpha,\alpha}\delta_{ij}$); and $|\dot{\gamma}|$ = magnitude defined as the second invariant of the shear rate tensor: $|\dot{\gamma}| = \sqrt{1/2\dot{\gamma}_{ij}\dot{\gamma}_{ij}}$. Eq. (7) can be derived from the mass conservation equation and the definitions of the dilatancy angle ψ and the strain γ (Andreotti et al. 2013). Eq. (8) is a closure relation, obtained by fitting the experimental measurements. In this study, K_3 was set to 4.09, according to Pailha and Pouliquen (2009).

Eqs. (7) and (8) describe the important role of the dilatancy played in adjusting the friction between solid particles: the dilation of a dense granular material ($\phi_s > \phi_{eq}$, $\psi > 0$) is accompanied by an increase of the interstitial pore volume of the granular material [because $(d\phi_s)/(dt) < 0$], which will result in a decrease of the pore pressure, or equivalently an increase of the effective normal stress acting on the solid skeleton. As a consequence, the frictional force between particles will increase according to Coulomb's friction law. This trend will continue until dilation disappears, i.e., $\phi_s = \phi_{eq}$ and $\psi = 0$. A similar analysis leads to the fact that the compaction of a loose granular material ($\phi_s < \phi_{eq}$, $\psi < 0$) will result in an increase of the pore pressure, or equivalently a decrease of the interparticle friction. This phenomenon is called pore pressure feedback (Iverson 2000, 2005) and will be shown in the present numerical simulation.

In order to close the momentum Eqs. (5) and (6), it is necessary to specify the constitutive relations for the intrinsic stress tensors, which will be described in the next subsection.

Constitutive Laws and Interaction Forces

In this study, the water phase was considered as a Newtonian fluid, thus the constitutive law for Newtonian fluid was applicable. In SPH method, the water is considered as a weakly compressible fluid, where the pore water pressure is calculated by the equation of state as (Monaghan 1994)

$$p = B\left[\left(\frac{\tilde{\rho}^l}{\tilde{\rho}^l_0}\right)^{\lambda} - 1\right] \tag{9}$$

where $\tilde{\rho}^l_0$ = referential true density of water; λ = constant normally set to 7; and B = problem-dependent parameter that sets a limit to the maximum change of water pressure.

Consider the soil as an elastic-perfectly plastic material with a Drucker-Prager yield criterion

$$F(I_1, J_2) = \sqrt{J_2} + \alpha_{\theta,\psi}I_1 - k_{c,\psi} \tag{10}$$

where I_1 = first invariant of the total soil stress tensor $\tilde{\boldsymbol{\sigma}}_s$; and J_2 = second invariant of the deviatoric soil stress tensor $\tilde{\boldsymbol{\tau}}_s$. Thus I_1 and J_2 are defined as

$$I_1 = \tilde{\sigma}_s^{xx} + \tilde{\sigma}_s^{yy} + \tilde{\sigma}_s^{zz}, \qquad J_2 = \frac{1}{2}\tilde{\tau}_s^{\alpha\beta}\tilde{\tau}_s^{\alpha\beta} \tag{11}$$

In Eq. (10), $\alpha_{\theta,\psi}$ and $k_{c,\psi}$ are constants that can be related to the cohesion c and the internal friction angle θ (as well as the dilatancy angle ψ if included) of the Mohr-Coulomb failure criterion (Bui et al. 2008). For plane strain problem, $\alpha_{\theta,\psi}$ and $k_{c,\psi}$ are determined by

$$\alpha_{\theta,\psi} = \frac{\tan(\theta+\psi)}{\sqrt{9+12\tan^2(\theta+\psi)}} \tag{12}$$

$$k_{c,\psi} = \frac{3c}{\sqrt{9+12\tan^2(\theta+\psi)}} \tag{13}$$

These two relations indicate that the change in volume fraction (i.e., dilatancy) implies an additional contribution to the frictional force due to the geometrical entanglement. Defining an apparent internal friction angle θ' as $\theta' \equiv \theta + \psi$, it can be seen that the dilatancy angle ψ plays the role of adjusting the apparent friction angle θ'. Thus dilatancy can not only adjust the effective normal stress acting on the solid skeleton through the pore pressure feedback regime as mentioned previously, it can also adjust the friction coefficient through the geometrical entanglement regime. Here it should be pointed out that for dry granular materials only the second regime is in effect, while for saturated granular materials both regimes exist simultaneously and influence the mixture dynamics drastically.

Two types of constitutive relation for the soil were implemented in the simulation, according to the plasticity flow rule used to describe how the plasticity deformation takes place once the stress threshold has been reached. In the case of associated flow rule, the constitutive law of soil reads

$$\begin{aligned}\dot{\tilde{\sigma}}_s^{\alpha\beta} - \tilde{\sigma}_s^{\alpha\gamma}\dot{\omega}_s^{\beta\gamma} - \tilde{\sigma}_s^{\gamma\beta}\dot{\omega}_s^{\alpha\gamma} &= 2G\dot{e}_s^{\alpha\beta} + K\dot{\varepsilon}_s^{\gamma\gamma}\delta^{\alpha\beta} \\ &\quad - \dot{\lambda}\left[3\alpha_{\theta,\psi}K\delta^{\alpha\beta} + G/\sqrt{J_2}\tilde{\tau}_s^{\alpha\beta}\right]\end{aligned} \tag{14}$$

where $\dot{e}_s^{\alpha\beta}$ = deviatoric part of the strain rate tensor $\dot{\varepsilon}_s^{\alpha\beta}$; G = shear modulus; and K = bulk modulus. The left-hand side is, in fact, the Jaumann rate, with $\dot{\omega}_s^{\alpha\beta}$ being the rotational rate tensor. The rate of change of plastic multiplier $\dot{\lambda}$ is calculated by

$$\dot{\lambda} = \frac{3\alpha_{\theta,\psi}K\dot{\varepsilon}_s^{\gamma\gamma} + (G/\sqrt{J_2})\tilde{\tau}_s^{\alpha\beta}\dot{\varepsilon}_s^{\alpha\beta}}{9\alpha_{\theta,\psi}^2 K + G} \tag{15}$$

In the case of nonassociated flow rule, the constitutive relation for soil is

$$\begin{aligned}\dot{\tilde{\sigma}}_s^{\alpha\beta} - \tilde{\sigma}_s^{\alpha\gamma}\dot{\omega}_s^{\beta\gamma} - \tilde{\sigma}_s^{\gamma\beta}\dot{\omega}_s^{\alpha\gamma} &= 2G\dot{e}_s^{\alpha\beta} + K\dot{\varepsilon}_s^{\gamma\gamma}\delta^{\alpha\beta} \\ &\quad - \dot{\lambda}\left[9K(\sin\psi)\delta^{\alpha\beta} + G/\sqrt{J_2}\tilde{\tau}_s^{\alpha\beta}\right]\end{aligned} \tag{16}$$

where the rate of change of plastic multiplier $\dot{\lambda}$ is

$$\dot{\lambda} = \frac{3\alpha_{\theta,\psi}K\dot{\varepsilon}_s^{\gamma\gamma} + (G/\sqrt{J_2})\tilde{\tau}_s^{\alpha\beta}\dot{\varepsilon}_s^{\alpha\beta}}{27\alpha_{\theta,\psi}K\sin\psi + G} \tag{17}$$

In the current study, a two-fluid SPH mixture model, combined with the critical state theory and the elastoplastic constitutive relations, were proposed to describe the dilatancy or compaction effects on the mixture dynamics. Interparticle friction enhancements by both the pore pressure feedback and geometrical entanglement regimes were taken into account in this model. It is the first time, to the best of the authors' knowledge, that such a combined model has been proposed for saturated mixture flows. This work is a further development of the work in Wang et al. (2017a, b). In Wang et al. (2017a), the friction angle θ was adjusted empirically, while in the current study, it was elegantly adjusted according to the critical state theory, i.e., Eqs. (12) and (13). In addition, the cohesion effect was considered in this study.

Numerical Methodology

SPH Model for Water-Soil Mixture

An in-house SPH code was developed to undertake the analysis presented here for the problem of submerged water jet soil excavation. In this section, the SPH implementation is not described in detail; only some special numerical treatments and improvements are presented instead. Interested readers are directed to Wang et al. (2016a) for more information.

In the following, the subscripts a and b represent the water particles, and i and j are the soil particles. The SPH approximation for the momentum equation of water is

$$\begin{aligned}\frac{d^l v_a^\alpha}{dt} &= -\phi_a\sum_b m_b\left(\frac{p_a}{\rho_a^2} + \frac{p_b}{\rho_b^2} + \Pi_{ab}\right)\frac{\partial W_{ab}}{\partial x_a^\alpha} \\ &\quad + \sum_b m_b\left(\frac{\tilde{\tau}_a^{\alpha\beta}\phi_a}{\rho_a^2} + \frac{\tilde{\tau}_b^{\alpha\beta}\phi_b}{\rho_b^2}\right)\frac{\partial W_{ab}}{\partial x_a^\beta} - \sum_i m_i\frac{f_{ia}^\alpha}{\rho_i\rho_a}W_{ia} + g_a^\alpha\end{aligned} \tag{18}$$

where Π_{ab} = artificial viscosity term added to prevent nonphysical penetration of particles (Monaghan 1994); $\mathbf{f}_{ia}$ = Darcy's drag force between water particle i and soil particle a; and W_{ab} is the kernel function used in SPH interpolation approximation, which was chosen as a Wendland quintic kernel function in this study (Wang et al. 2016a).

The model uses both artificial and physical viscosity in the water momentum balance equation. This combined use is frequently avoided in dealing with rapidly varied flows (Amicarelli et al. 2017). For the submerged water jet excavation, artificial viscosity was added to prevent particle penetrations but was so small that it had little effect on the overall performance of the numerical simulation.

The SPH approximation of the momentum equation of solid can be derived analogously, however, with the buoyancy force $-\phi_s\nabla p$ at solid particle i replaced by

$$-\phi_i\nabla p_i \approx -\phi_i\sum_a\frac{m_a}{\rho_a}(p_a - p_i')\frac{\partial W_{ia}}{\partial x_i^\alpha} \tag{19}$$

where p_i' = pore water pressure at the location of solid particle i, obtained by using the normal SPH interpolation approximation

$$p_i' \approx \sum_a\frac{m_a}{\rho_a}p_a W_{ia} \tag{20}$$

Here, p_i' is introduced to obtain an antisymmetric discretization of the pore pressure gradient term, which can avoid pore pressure jump at the water-soil interface. This numerical instability, in some cases, may lead to failure of the SPH application to submerged granular flows (Bui et al. 2011).

Eq. (19) can also be derived using the transformation

$$-\phi_i \nabla p_i = -\phi_i(\nabla p_i - p_i' \nabla 1) \approx -\phi_i \sum_a \frac{m_a}{\rho_a}(p_a - p_i')\frac{\partial W_{ia}}{\partial x_i^\alpha} \tag{21}$$

which suggests that adding the term p_i' does not cause any inconsistency in the gradient approximation for the pore water pressure. Eq. (21) introduces pressure difference (i.e., relative pressure) into the discrete particle approximation, and is usually preferred in SPH formulations.

The momentum equation for solid is thus approximated as

$$\frac{d^s v_i^\alpha}{dt} = \sum_j m_j \left(\frac{\tilde{\sigma}_i^{\alpha\beta}\phi_i}{\rho_i^2} + \frac{\tilde{\sigma}_j^{\alpha\beta}\phi_j}{\rho_j^2} + \Pi_{ij}\delta_{\alpha\beta}\right)\frac{\partial W_{ij}}{\partial x_i^\beta} - \phi_i \sum_a \frac{m_a}{\rho_i \rho_a}(p_a - p_i')\frac{\partial W_{ia}}{\partial x_i^\alpha} + \sum_a m_a \frac{f_{ia}^\alpha}{\rho_i \rho_a} W_{ia} + g_i^\alpha \tag{22}$$

Volume fraction ϕ_a for a water particle a is calculated according to

$$\phi_a = 1 - \sum_j \frac{m_j}{\rho_j}\phi_j W_{aj} \tag{23}$$

where the summation term gives soil volume fraction ϕ_s at the position of water particle a. From Eq. (23), we also obtain

$$\frac{d^l \phi_a}{dt} = -\sum_j \frac{m_j}{\rho_j}\phi_j v_{aj}^\alpha \frac{\partial W_{aj}}{\partial x_a^\alpha} \tag{24}$$

which is actually the SPH approximation of the relation $d^l\phi_l/dt = -d^l\phi_s/dt$. In the current study, Eq. (24) was used in each time step to calculate $(d^l\phi_a)/(dt)$, which was then used to get the value of ϕ_a by time stepping. In this study, a reinitialization technique was employed for the calculation of ϕ_a, that is, after every several time steps, ϕ_a was recalculated using Eq. (23). With this reinitialization technique, the calculation was stable, and the large gradient of ϕ_a at the interface of the water-soil mixture and the ambient water can still be retained satisfactorily, which will be shown subsequently.

Particles Shifting

In SPH, particles move along streamlines due to the Lagrangian nature of this method. This may create problems in the particle distribution, which can ultimately lead to the simulation breakdown, when nonphysical voids or cavities are created as particles clustering together in an anisotropic manner, making the SPH kernel support no longer complete. This will be shown subsequently. Xu et al. (2009) and Shadloo et al. (2012) showed that introducing a particle-shifting correction can prevent errors due to irregular particle distributions. Lind et al. (2012) further extended the shifting formulation for free-surface flows based on Fick's law in order to stabilize the particle motion and homogenize their distribution in space. The key idea of the particle shifting is to modify the particle positions x_i as follows (Vacondio et al. 2013):

$$\frac{\mathrm{d}\mathbf{x}_i}{\mathrm{d}t} = \mathbf{v}_i + \delta\mathbf{v}_i \tag{25}$$

where $\delta\mathbf{v}_i = i$th particle shifting vector given by

$$\delta\mathbf{v}_i = \frac{\chi}{m_T}\sum_j m_j \frac{\mathbf{r}_{ij}}{r_{ij}^3} r_0^2 v_{\max} \tag{26}$$

in which $r_0 = \sum_j r_{ij}/N$; $m_T = \sum_j m_j$; χ = nondimensional parameter; $v_{\max}$ = maximum velocity magnitude in the system; and $\mathbf{r}_{ij} = \mathbf{r}_i - \mathbf{r}_j$. In this study, χ was set to 0.01 according to Xu et al. (2009) and Vacondio et al. (2013).

Treatment of Plasticity

In this paper, the soil was modeled as an elastic-plastic material whose constitutive law contains plasticity terms, as seen in Eqs. (14) and (16). These terms need to be computed only when the stress state is outside of the yield surface.

That means, in each time step, the elastic part of the stress rate $\dot{\tilde{\sigma}}_{\alpha\beta}^*$ is calculated first and then the stress state at the next step $\tilde{\sigma}_{\alpha\beta}^*$ is predicted using the one-step-forward Euler method as

$$\tilde{\sigma}_{\alpha\beta}^* = \tilde{\sigma}_{\alpha\beta}^n + \dot{\tilde{\sigma}}_{\alpha\beta}^* \Delta t \tag{27}$$

Then the yielding state of the predicted stress $\tilde{\sigma}_{\alpha\beta}^*$ is determined by the Drucker-Prager criterion in Eq. (10). If it is outside of the yielding surface, the stress rate will be updated by adding the plastic part of the stress rate (i.e., the terms with plasticity multiplier $\dot{\lambda}$)

$$\dot{\tilde{\sigma}}_{\alpha\beta} = \dot{\tilde{\sigma}}_{\alpha\beta}^* + \dot{\tilde{\sigma}}_{\alpha\beta}^{pl} \tag{28}$$

This corrected stress rate $\dot{\tilde{\sigma}}_{\alpha\beta}$ is then used to update the stress at the next step with other fundamental variables by means of a second-order leapfrog time-stepping algorithm. With this approach, the stress rate can be determined explicitly. It is also convenient to apply other kinds of solid constitutive relationships with rate dependency, i.e., historic memory, within this framework.

Boundary Conditions

The determination of boundary conditions in the SPH method is important and yet a challenging topic because of the Lagrangian nature of the method. When a particle moves close to the boundary of the domain, the kernel function W_{ab} will be truncated by the boundary, and the SPH approximation is no longer accurate, leading to the so-called problem of boundary deficiency. To overcome this deficiency, several types of boundary treatment methods have been developed, such as repulsive particles (Monaghan 1994), ghost particles (Libersky and Petschek 1991), artificial particles (Morris et al. 1997), and dynamic particles (Crespo et al. 2007; Gomez-Gesteira et al. 2012), according to their characteristics. More advanced boundary treatment methods can be seen in Monaco et al. (2011), Amicarelli et al. (2013), and Ferrand et al. (2013), where a general semianalytic approach for modeling solid boundaries in the SPH method is proposed.

In this paper, the wall boundaries, including the tank wall and the nozzle wall, were treated by the dynamic particle method, as seen in Fig. 1. The main feature of these particles is that they satisfy the same equations as the real particles. While remaining fixed in position (for fixed boundaries) or movable according to some externally imposed movements (for moving objects like gates and wave makers), their physical variables, including density and pressure, evolved with time according to the corresponding governing equations. Because of this feature, they are called dynamic. This method is easy to implement since the dynamic particles can be calculated inside the same loops as real particles with a considerable saving of computational time.

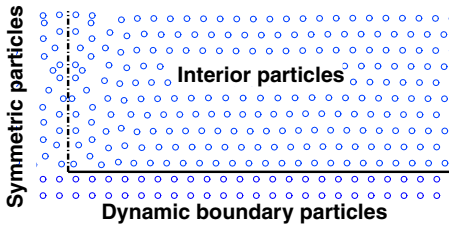

Fig. 1. Wall boundary and symmetric boundary treatments in the present SPH simulation.

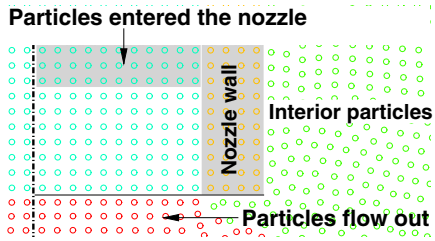

Fig. 2. Inlet boundary treatment in the present SPH simulation.

Due to the symmetry of the computation domain, a symmetric boundary was also introduced to reduce the computational cost. The symmetric boundary was treated by the mirror particle method, as also illustrated in Fig. 1. These particles were generated at runtime and their positions and variables were obtained simply by mirror reflection of their real counterparts in the fluid domain.

During the jetting process, water particles flow into the tank through the nozzle. Particles in the nozzle were treated as dynamic particles, i.e., their velocities were set to be the jet velocity while other variables evolved as real particles. When they entered the tank, they became real particles and the same amount of dynamic particles were then generated at the entrance of the nozzle as substitutes, as illustrated in Fig. 2. In this way, the number of water particles in the nozzle remained constant.

In this paper, the water level in the tank was kept not higher than the tank side wall after the tank was filled. Since water particles enter the tank from the nozzle continuously, to keep a fixed amount of water in the tank, particles must overflow from the tank when they reach the free surface. To treat the overflow condition, particles that exceed the free surface were removed from the computation. That is, they were not used as active particles in the computation any longer. It was found that such a simple treatment about overflow condition does not result any unstable phenomenon.

Reinitialization of Water Volume Fraction

The interface of the water-soil mixture and the ambient water was in fact a singular surface for the water volume fraction ϕ_l, which jumps across the interface from a lower value in the mixture to a unit in the ambient fluid. In discretized form, the interface thus represents an abrupt transition zone of ϕ_l. Due to numerical dissipation, this transition zone might become wider and wider along with the time stepping, leading to a smoothed variation of ϕ_l across the interface, as seen in Fig. 3, which shows a mixture flow submerged in water. To remedy this, a reinitialization technique, commonly used in the SPH method (Gomez-Gesteira et al. 2012), was applied to the calculation of ϕ_l. In doing so, ϕ_l was recalculated using Eq. (23) every several time steps. With this reinitialization

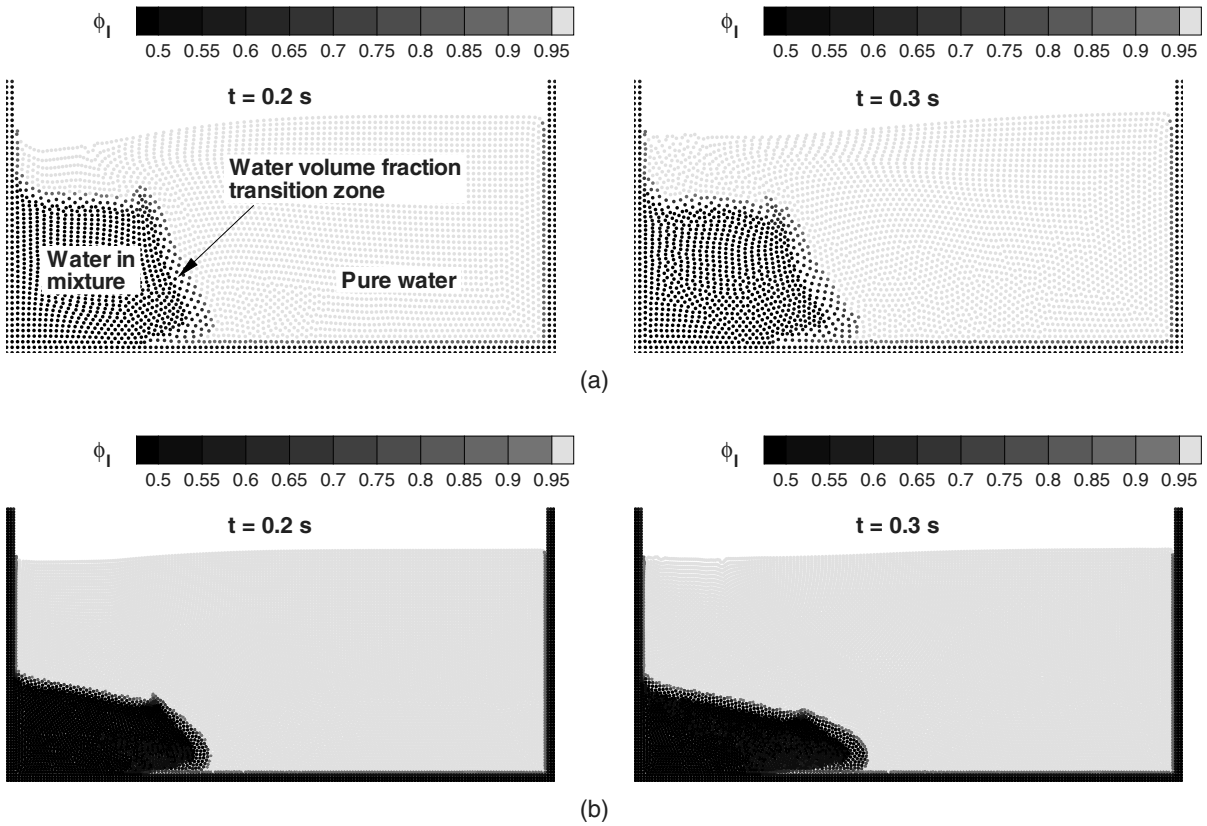

Fig. 3. Simulation of water volume fraction: (a) without; and (b) with the reinitialization technique, for the case of a submerged mixture flow.

J. Hydraul. Eng., 2019, 145(6): 04019016

technique, the transition zone was kept narrow, namely, the abrupt change of the water volume fraction ϕ_l at the interface was maintained, as shown in Fig. 3.

Parallel Computing

The main disadvantage of particle-based methods is that they require a very large number of particles to obtain reliable numerical results. Fortunately, it is relatively easy to parallelize particle methods and the massive parallel computation capabilities of modern graphics processing units (GPUs) now make it possible to simulate large systems at acceptable computational costs. Our SPH code is parallelized using OpenACC, with the particle neighbors searching using Thrust. OpenACC emerged in 2011 as a programming model that uses high-level compiler directives to expose parallelism in the code and to build the parallel code for a variety of accelerators. Thrust is a parallel algorithms library that resembles the C++ Standard Template Library (STL). Its high-level interface greatly enhances programmer productivity while enabling performance portability between GPUs and multicore CPUs. The SPH code used in this study was developed using the FortranN programming language under the environment of the PGI Fortran compiler.

Computing with a GPU, it is not necessary to store the neighboring particle list. The neighboring particles are searched when needed. A fast searching technique is thus very important. Aided by a background grid, the searching process consists of three steps, i.e., the (cellID, particleID) hash table setup, the radix sort of the hash table by the key cellID using Thrust, and scanning for the start and end position of each cellID in the sorted hash table. All these can be done efficiently within the GPU in parallel manner. Communication between the GPU and CPU is only needed for postprocess, thus this overhead is kept to a minimum.

Simulations and Results Analysis

Scour by Plane Horizontal Wall Jet

In this section, a local scour caused by a two-dimensional (2D) plane wall jet is considered. Fig. 4 is a definition sketch for the numerical model. The 2D rectangular tank containing water-soil mixture was 4 m in length and 2 m in height. The thickness of the water-soil mixture was 1 m. The nozzle had a width of $D_j = 0.1$ m. The velocity of the water jet V_j was 5 m/s. The main factors studied were the maximum depth of erosion ϵ_m occurring at a distance of x_m from the nozzle, as well as the characteristics of the dune that forms at the downstream end of the scour hole, in terms of maximum height $\Delta\epsilon$ and position x_c. All these variables are functions of time, as the profile of the scour hole evolves during the scour process. Their values at the asymptotic (or equilibrium) state are denoted by $\epsilon_{m\infty}$, $x_{m\infty}$, $\Delta\epsilon_\infty$, and $x_{c\infty}$, respectively. In this paper, numerical simulations were conducted to study the time development of the scour.

There were initially a total of 13,248 fluid particles and 6,552 solid particles generated regularly for the water and solid phases in the tank, respectively. The initial particle spacing was 0.025 m. Time step size $\Delta t = 5 \times 10^{-6}$ s. Material properties used in the calculation are given in Table 1. Here, an initially dense packing soil was considered. For this case study, the soil was cohesionless.

The velocity field of the water phase during the scour process is shown in Fig. 5. At the initial stage of the scour, due to the asymmetric entrainment of the surrounding fluid, the main stream of the water jet deflected upward, resulting in two counterrotating vortices on both sides of it. Along with the erosion of the bed surface, a scour hole developed and a third small vortex formed in it, just beneath the main stream. The strength and position of these vortices were variable with the development of the scour hole, leading to a jet flow oscillating between a position along the bed and a position in the horizontal direction, which is consistent with the experimental observations of Aderibigbe and Rajaratnam (1998). Movement of water jet particles predicted by the SPH numerical model at representative times are shown in Fig. 6. Water jet deflection and entrainment of the surrounding water were well predicted by the proposed SPH numerical model.

Fig. 7 shows the profiles of the scour hole at representative times. Only short-term evolution of the scour hole is given here

Table 1. Material properties used in the computation of submerged water jet excavation

Property	Value
True density of soil, $\tilde{\rho}_s$ (kg/m^3)	2,700
Young's modulus of soil, E (MPa)	150
Poisson's ratio of soil, ν	0.3
Internal friction angle of soil, θ (degrees)	20
Initial volume fraction of soil, ϕ_{s0}	0.55 (loose packing) 0.60 (dense packing)
Equilibrium volume fraction of soil, ϕ_{eq}	0.58
Hydraulic conductivity of soil, k (m/s)	0.001
Viscosity of water, μ (Pa · s)	0.001
Initial true density of water, $\tilde{\rho}_{f0}$ (kg/m^3)	1,000
Parameter K_3 in Eq. (8)	4.09
Cohesion of soil, c (kPa)	0–25

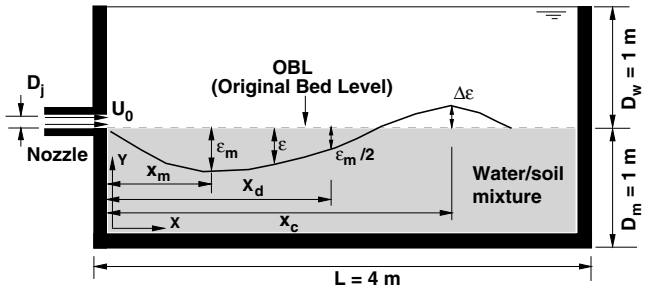

Fig. 4. Submerged plane wall jet scour.

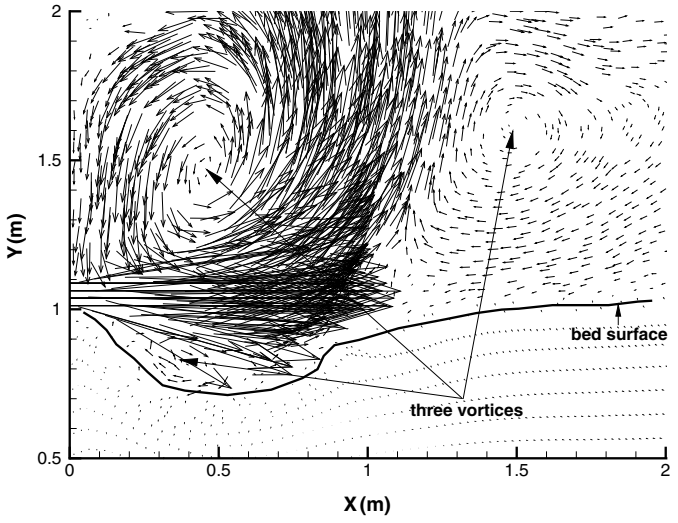

Fig. 5. Velocity vectors of water particles during the process of scour.

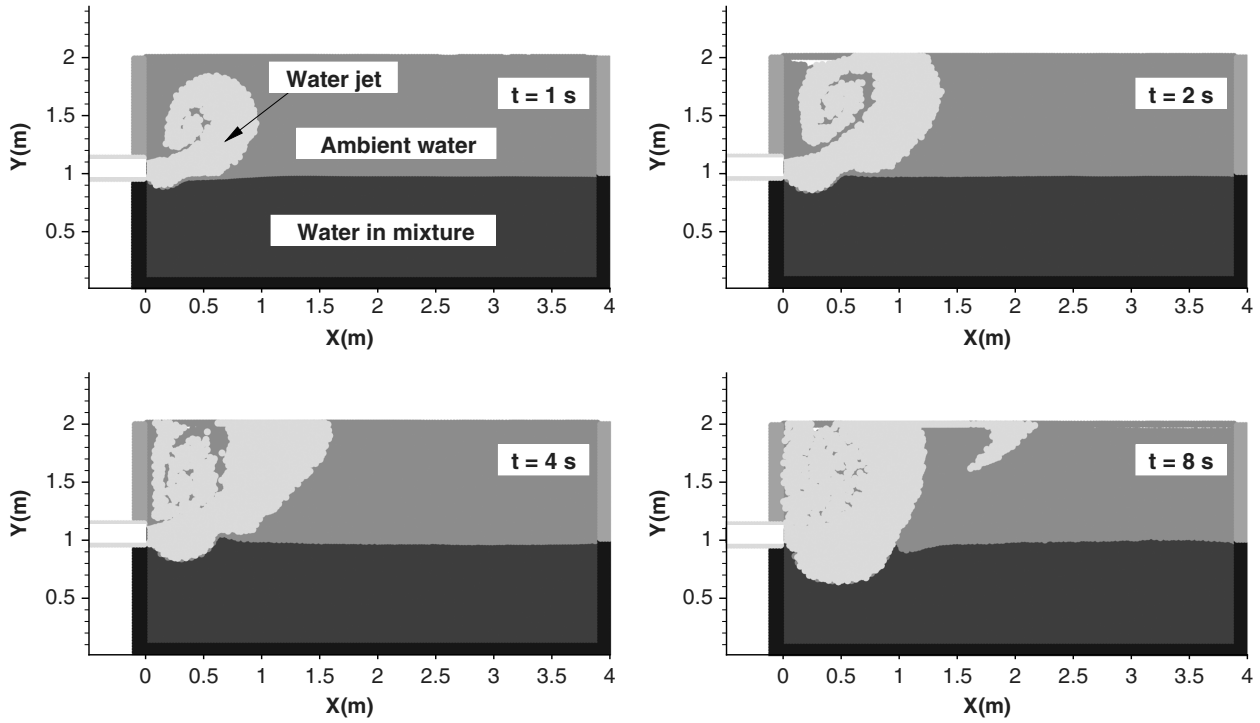

Fig. 6. Movement of the water jet particles.

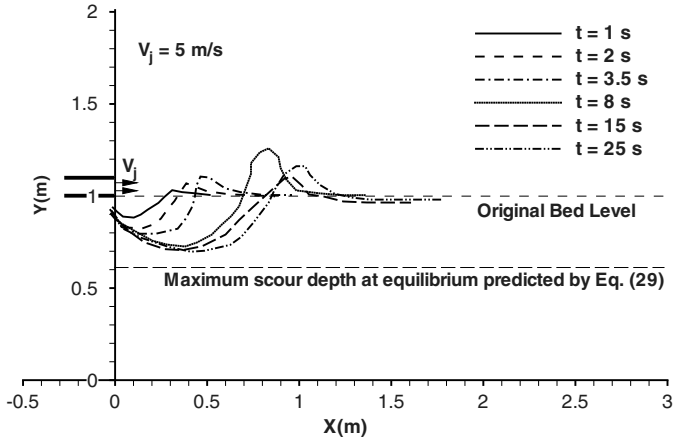

Fig. 7. Scour profiles at representative times.

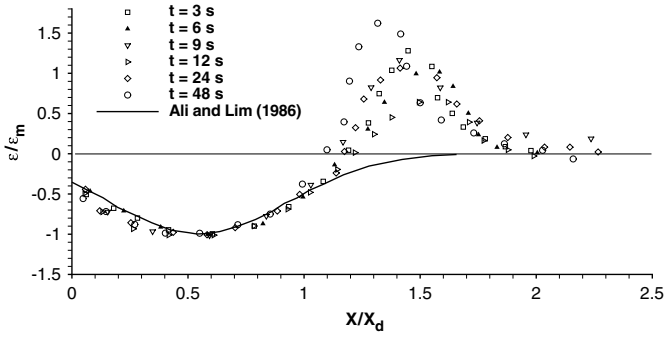

Fig. 8. Dimensionless scour profiles at representative times.

because of the time-consuming computation process. Chatterjee et al. (1994) proposed an empirical equation for the maximum scour depth at equilibrium as

$$\frac{\epsilon_{m\infty}}{D_j} = 0.775\mathrm{F}_j \tag{29}$$

where F_j = Froude number, $\mathrm{F}_j = V_j/(gD_j)^{1/2}$. It is seen that the SPH numerical results qualitatively agree with that predicted by Eq. (29).

Rajaratnam (1981), Ali and Lim (1986), Ali and Neyshaboury (1991), Mazurek et al. (2003), and many others conducted experimental studies on this topic. They showed that the scour patterns caused by jets were similar in shape as the scour progressed, and thus could be described by a single parameter. Fig. 8 shows the dimensionless shape of a scour hole with time evolution. As a result of this, the parameter x_d, the distance from the jet exit to the point where $\epsilon = \epsilon/2$, can be used to describe the bed configuration.

Although long-term simulation to the equilibrium state is hard to reach in the numerical simulation, it is still helpful to investigate the performance of the proposed SPH model in a long-term simulation. Fig. 9 compares the scour profile at $t = 48$ s given by the SPH method with the experimental observations of the scour hole at the equilibrium state. In this figure, the distance from the nozzle to the crest of the dune, x_c, is taken as the characteristic length to normalize the longitudinal coordinate. It is seen that the long-term simulation of the SPH model is still acceptable, compared with the experimental observations. The validity of the proposed SPH model is thus demonstrated.

Excavation by Plane Impinging Water Jet

As seen in Fig. 10, the 2D rectangular tank containing water-soil mixture was 0.6 m in length and 0.4 m in height. The tank was partially filled with water. The initial water level D_w was 0.3 m.

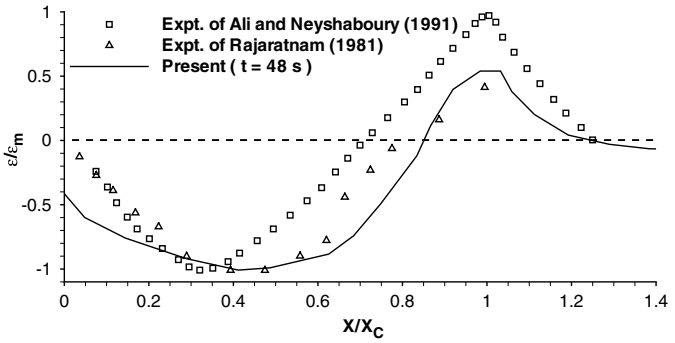

Fig. 9. Dimensionless scour profile at $t = 48$ s, compared with the experimental observations at equilibrium.

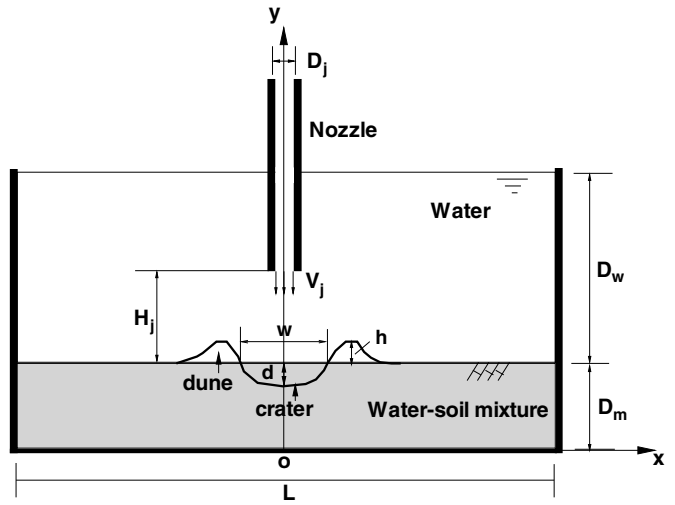

Fig. 10. Submerged impinging water jet excavation.

At the bottom of the pure water, there was a layer of water-soil mixture $D_m = 0.1$ m thick. The inflow boundary corresponding to the submerged vertical water jet (plane in 2D space) had a width of D_j (m), placed H_j (m) above the initial soil surface. The water jet had a constant speed of V_j (m/s). Jetting began at $t = 0$. After a period of time, a crater with dunes formed in the granular bed due to the impingement of the water jet. The width of the tank was two to three times larger than the crater width. Numerical simulation showed that soil near the side wall was almost static, i.e., the soil surface there was almost unchanged. Thus the side wall had negligible effects on the soil deformation. The granular bed was also thick enough that the bottom wall effect was also negligible.

In this study, the water level D_w in the tank was kept constant and treated with the overflow condition. Infiltration or suction from the tank wall during the excavation was not considered. The initial water content, i.e., the water volume fraction ϕ_l, in the granular-water mixture was designated. During the excavation process, the water content was variable and evolved with the mixture flow due to the relative motion between solid and fluid particles.

Material properties used in the calculation are given in Table 1. Here, an initially loose packing soil was considered first. Dilatancy effects of dense packing soil will be investigated subsequently. Whether the soil was loose or dense was indicated by the initial volume fraction of the soil ϕ_{s0} relative to its equilibrium value ϕ_{eq}. In this paper, only laminar flow was considered because for the water jet excavation, the turbulence mixing region was small.

There were initially a total of 59,200 fluid particles and 21,120 solid particles generated regularly for the water and solid phases in the half tank, respectively. The initial particle spacing was 0.00125 m. Numerical parameters were chosen as follows. The virtual speed of sound for water $c_f = 10$–20 m/s and the speed of sound for soil $c_s = 215$ m/s. The artificial viscosity parameters were taken as $\alpha = 0.1$ and $\beta = 0$. The artificial diffusive parameter in δ-SPH method was set as $\delta = 0.1$ for both phases. For the repulsive force, $D = 0.01$ and $r_0 = 0.00125$ m. The time step size $\Delta t = 2.5 \times 10^{-6}$ s. For the meaning of the preceding numerical parameters, please refer to Wang et al. (2016a). The nonassociated flow rule with dilatancy angle given by Eq. (8) was implemented in the calculation.

The jetting process was simulated by using the proposed two-fluid SPH mixture model. Numerical simulation showed several interesting characteristics of the submerged water jet excavation. First, a pair of vortices can be seen at both sides of the jet core region. As shown in Fig. 11, the vortices initiated at the beginning of the jetting, and transported downward along with the jet. During this period, the size of the vortices became larger and larger due to the entrainment of the surrounding water. When impacting the soil surface, the jet current deflected toward both sides along the soil surface, which itself was undergoing deformation under the impingement of the jet. The jet current was then almost reversed by the curved crater profile.

Second, the contour plot for the water velocity component v_y is given in Fig. 12. It is seen that, in this case, the length of the jet potential core region was about three times the nozzle width D_j. The potential core region was the one close to the nozzle exit. Water velocity in this region remained about the same as that at the nozzle exit. Since the jet core region cannot touch the soil surface, the excavation capacity was limited. Most of the kinematic energy of the water particles was dissipated by the entrainment of surrounding water. Only the laminar water jet was considered here. The length of the jet potential core region depends on the Reynolds number $V_j D_j/\nu_l$ and the relative impinging height H_j/D_j. In Beltaos and Rajaratnam (1973), a plane turbulent impinging air jet was considered, where a much longer potential core region (about 6.2–6.5 times D_j) was observed. The Reynolds number of the water jet in the present simulations was much higher than that of the air jet used in the experiments. Thus the turbulence intensity made a big difference in jet performance. In addition, the relative impinging height in the simulations was also much smaller than that used in the experiments, which also may be one of the reasons for the numerical discrepancy.

Third, as mentioned previously, in the case of high-velocity jetting, numerical simulation with SPH results in unphysical voids in the flow field. This is illustrated in Fig. 13. It can be seen that a pair of symmetric voids (i.e., the white regions without particles in the figure) forms near the nozzle exit at the initial stage of the jetting and becomes larger and larger during the jetting process, leading to an unphysical simulation of the water jetting. To remedy this, the particle shifting technology was employed, as seen in Eq. (26). The mechanism of this technology is to diffuse more water particles into the voids and prevent the irregular particle distributions. Fig. 13 compares the flow fields near the nozzle exit before and after using the particle shifting technology. It was observed that particles were diffused into the voids efficiently by the employed particle shifting technology. Although the positions of the particles were shifted, the velocity of the particles remained. Thus, the conservation of momentum was assured.

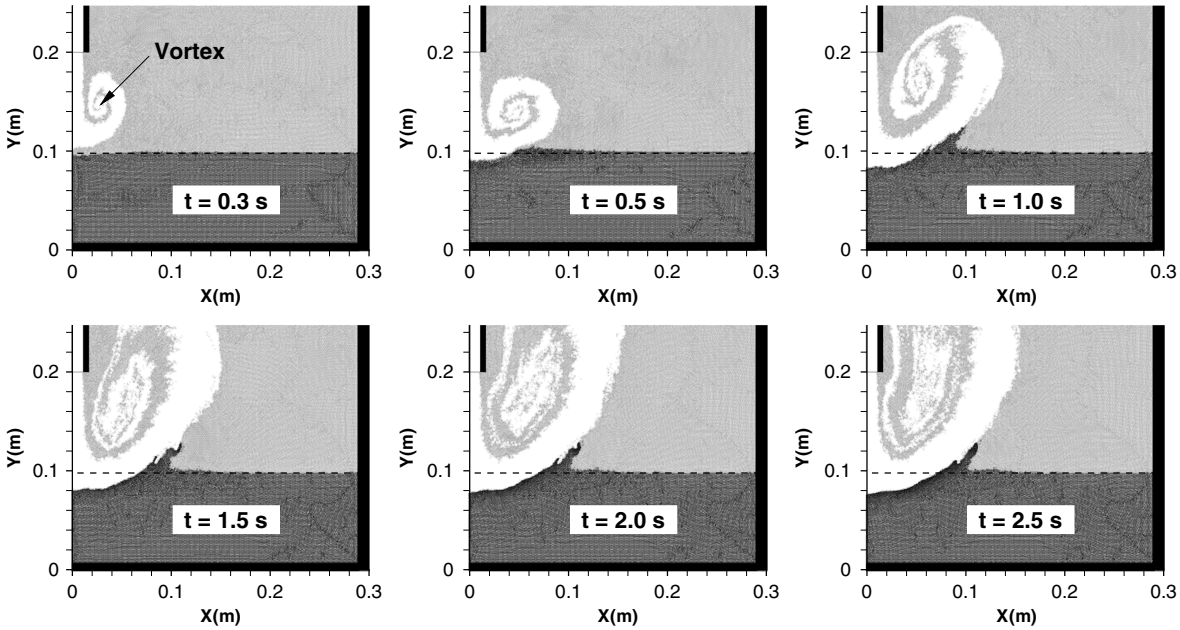

Fig. 11. Flow of water particles at the initial stage of the excavation, in the case of $D_j = 0.02$ m, $H_j = 0.1$ m, and $V_j = 1$ m/s. White indicates the water particles issued from the nozzle; gray indicates the water particles originally in the tank; and black indicates water particles in the mixture.

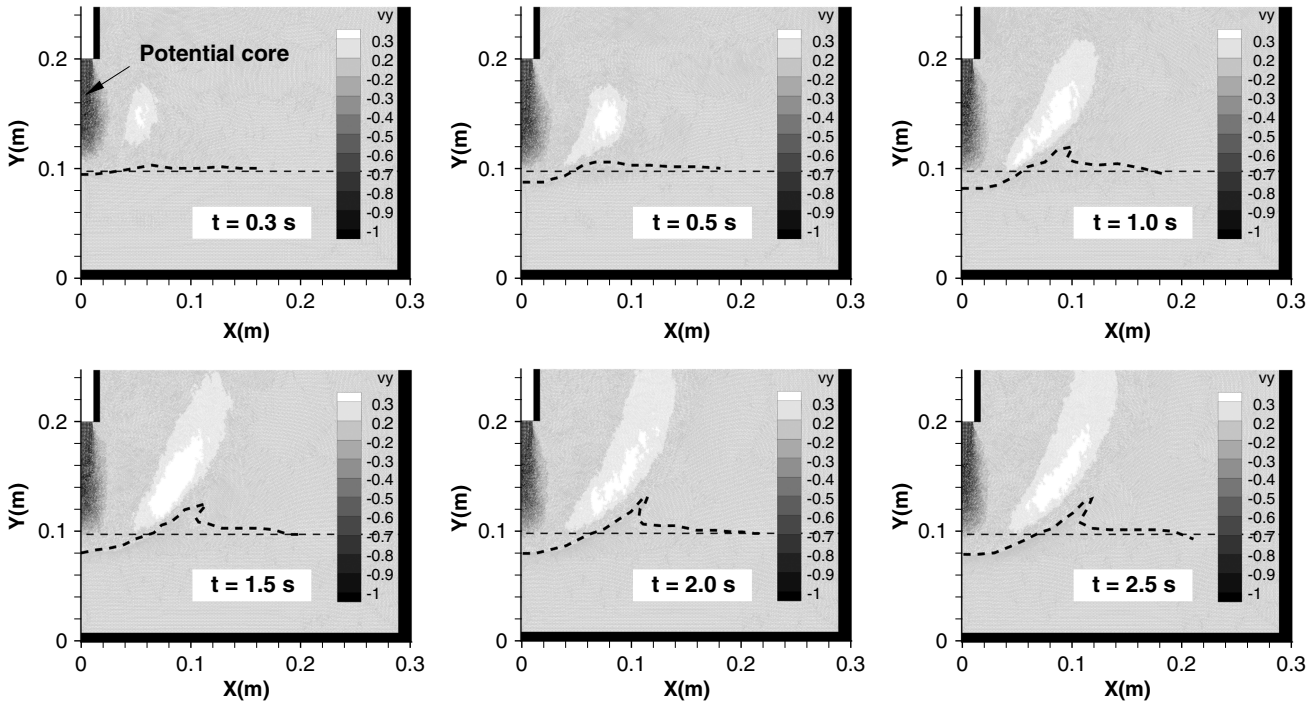

Fig. 12. Velocity component v_y of water particles at the initial stage of the excavation ($D_j = 0.02$ m, $H_j = 0.1$ m, $V_j = 1$ m/s). The dashed lines indicate the initial and deformed interfaces between the pure water upper layer and the mixture lower layer.

Verification of the Two-Fluid SPH Analysis

Fig. 14 compares the numerical excavation profiles with the experimental measurements of Akashi and Saito (1980). It can be seen that the present numerical results agree well with the experimental measurements. Not only the width and depth of the crater but also the size and position of the dune are well predicted. In addition, it can be seen that the excavation depth increases rapidly in the first few seconds, followed by slow erosion. Thus soil excavation under the water jet impingement develops in two stages. At the beginning of the excavation, the soil breakage happens due to the soil failure mechanism, which is characterized by the fast sliding of soil along the shear band. Then at the later stage, the erosion mechanism becomes dominant and the solid particles at the soil surface are driven to move due to the shear force of the water.

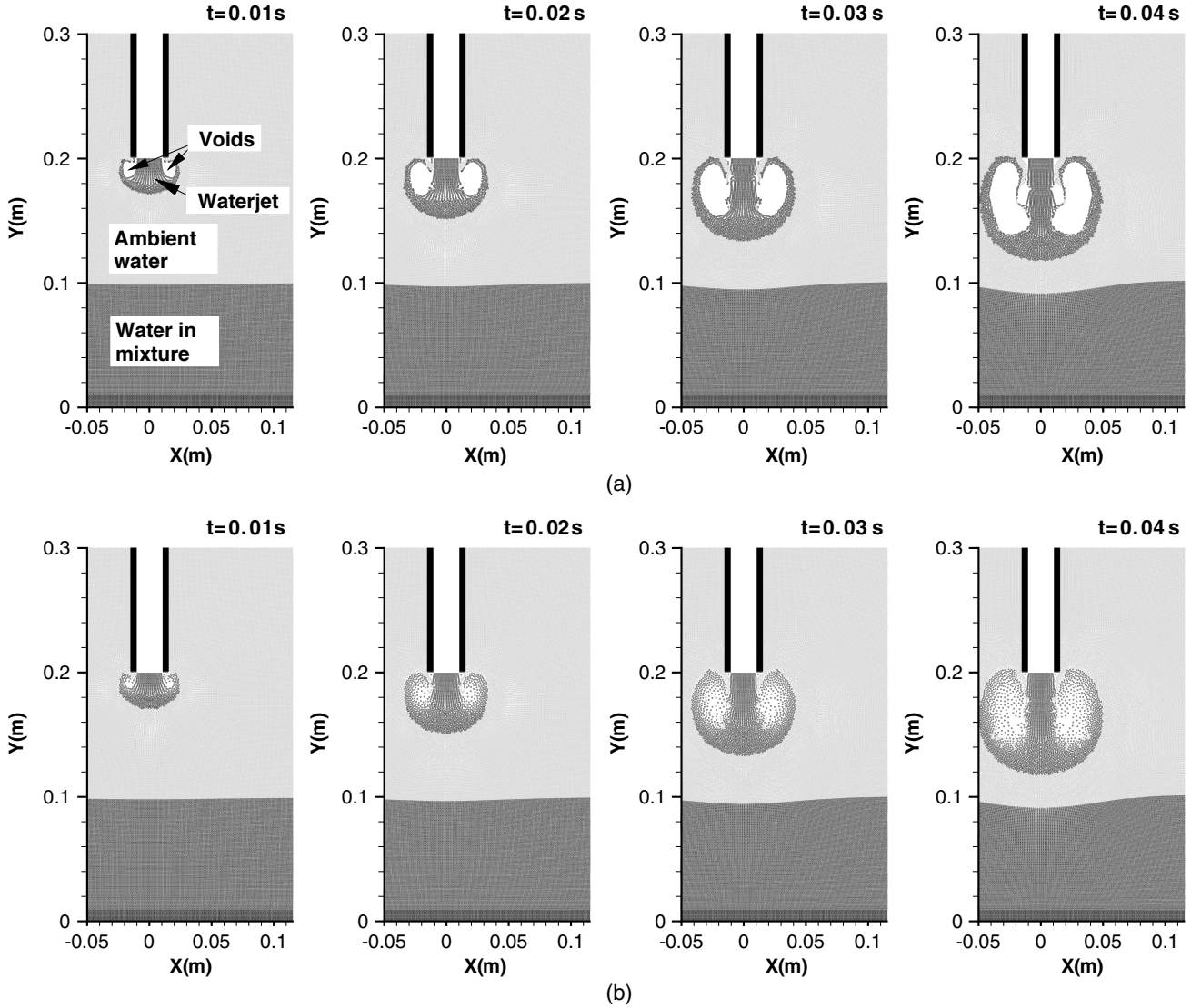

Fig. 13. Flow of water particles near the nozzle exit: (a) with; and (b) without using particle shifting technology ($D_j = 0.02$ m, $H_j = 0.1$ m, $V_j = 1$ m/s). For completeness, the symmetric part of the flow field is also shown.

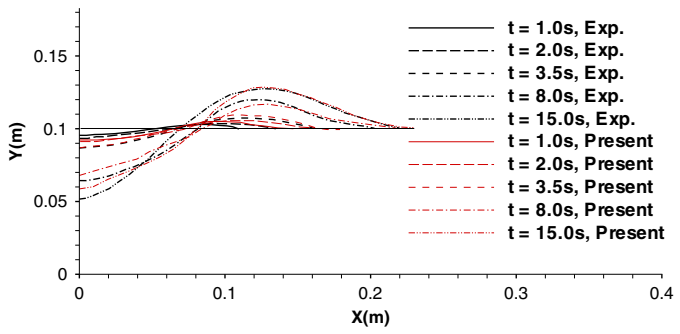

Fig. 14. Crater profile comparison between numerical results given by the present SPH method and the experimental measurements of Akashi and Saito (1980), in the case of $D_j = 0.02$ m, $H_j = 0.1$ m, and $V_j = 0.74$ m/s.

Fig. 15 compares excavation profiles predicted by different numerical approaches. Ikari et al. (2015) presented an moving particle semi-implicit (MPS) method-based simulation of excavation due to a submerged vertical jet with a sub-particle-scale suspended load model. Numerical results given by the commercial numerical software Fluent (Yuan et al. 2018) are also shown for comparison. It is seen that the shapes of the crater obtained by the proposed SPH model show good agreement with the ones given by the MPS method, especially at the initial stage. The discrepancy at a later stage may be due to the particle suspension. In fact, during the second stage of the excavation, a large number of solid particles suspended in the crater can be observed from the present SPH numerical simulations. The sub-particle-scale suspended load model used by Ikari et al. (2015) in MPS simulation may help to move these particles, as demonstrated in Fig. 15. While Fluent gives a moderate crater depth, the position of the dune is not satisfactory. In granular flows with high solid volume fraction, Fluent uses Schaeffer's expression (Schaeffer 1987)

$$\mu_{fr} = \frac{p_s \sin\theta}{2\sqrt{I_2(\dot{e}_{ij})}} \tag{30}$$

to account for the friction between particles, where p_s = solid pressure; and I_2 = second invariant of the deviatoric strain rate tensor $\dot{e}_{ij}$. This frictional stress is then added to the stress predicted by the kinetic theory when the solids volume fraction exceeds a

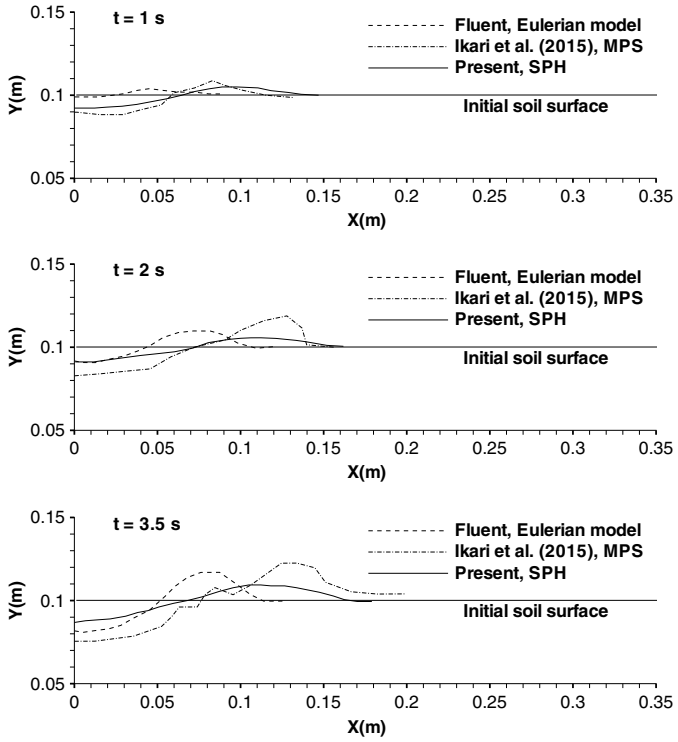

Fig. 15. Crater profiles compared with other numerical models, in the case of $D_j = 0.02$ m, $H_j = 0.1$ m, and $V_j = 0.74$ m/s.

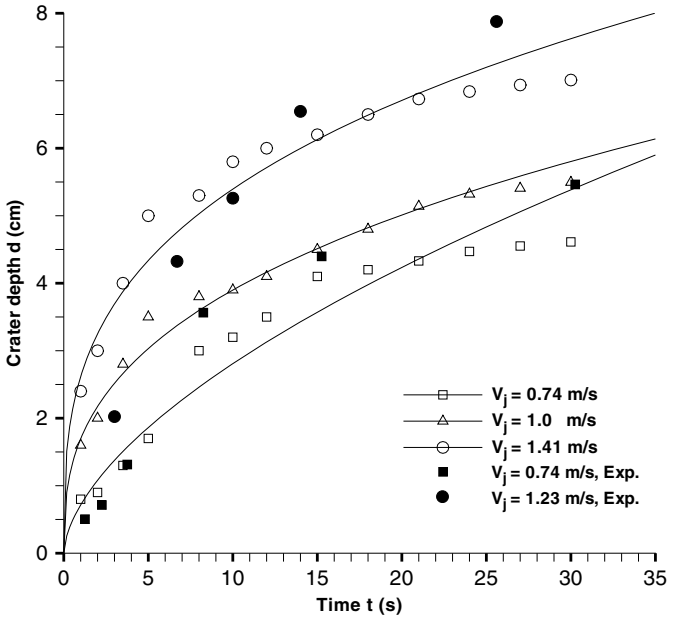

Fig. 16. Crater depth evolution under different jetting velocities V_j, in the case of $D_j = 0.02$ m and $H_j = 0.1$ m. The lines are guides for the eyes. Experimental results of Akashi and Saito (1980) are also given for comparison.

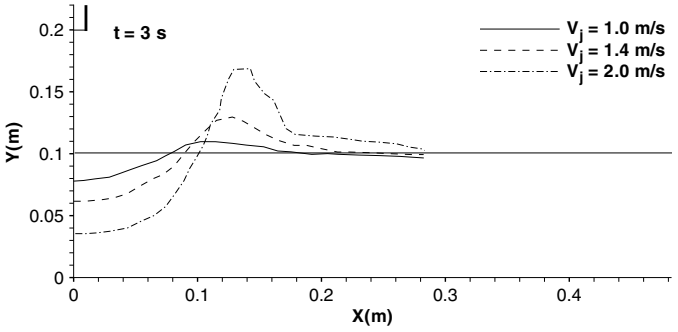

Fig. 17. Crater profiles under different jetting velocities V_j, in the case of $D_j = 0.02$ m, $H_j = 0.1$ m, and $t = 3$ s.

certain critical value. However, Schaeffer (1987) pointed out that the governing equations that include the expression for the friction viscosity in Eq. (30) are ill posed, which may be the reason Fluent cannot predict the excavation process satisfactorily.

As seen in Figs. 14 and 15, the depth of the crater in this paper is underestimated in comparison with experimental results and the MPS model. For the excavation problem considered here, the instantaneous deformation and failure of the granular material is concerned. It is assumed in the present study that the particle-particle friction make up the dominant contribution to the total stress associated with granular material. The contribution associated with the suspension, sedimentation, and instantaneous collision is less important and negligible compared with the interparticle friction. However, at the later stage of the excavation, these loads show their importance gradually and the resulting stresses need to be taken into account. Another reason may be due to the turbulence behavior of the water jet, which is not taken into consideration in this model. Although some reasons accountable for the underestimation of the crater depth are proposed here, they still need to be investigated carefully in the future.

Excavation Performance Analysis

In engineering practice, the excavation capability of the water jet is of great importance. In this section, the effects of jetting velocity V_j, nozzle width D_j, and impact distance H_j on the excavation performance are investigated.

Fig. 16 shows the time evolution of the crater depth at $x = 0$ (the impingement point) under different jetting velocities, compared with the experimental measurements of Akashi and Saito (1980). In this case, the nozzle width D_j and the impact distance H_j were fixed at 0.02 and 0.1 m, respectively. It is seen that, during the first few seconds, the depth increased rapidly, while at the later stage the depth increased slowly to its equilibrium state. In fact, it takes a very long time, say more than 1 h, to reach the equilibrium state, as observed in the physical experiments of Akashi and Saito (1980). In the current numerical simulation, excavation processes of tens of seconds were given and evolutions of the crater size during the later stage were only creeping. For most of the engineering applications, excavation performance at the first few seconds is of great importance. Thus, from now on, only the short-term evolution of the crater size is a concern, while the long-term evolution will not be demonstrated. A good agreement on the short-term evolution of crater depth between the numerical simulations and the experimental observations can be seen in Fig. 16.

Fig. 17 shows the crater profiles at $t = 3$ s for different jetting velocities. It is seen that with the increase of jetting velocity, the depth of the crater increases remarkably. Approximately, the short-term crater depth (e.g., for $t = 3$ s) is in the order of magnitude $O(V_j^2)$. Thus increasing the jetting velocity is an efficient way to enlarge the crater depth.

Although the maximum velocity in the preceding calculations was 2 m/s, much larger jetting velocities are still applicable in

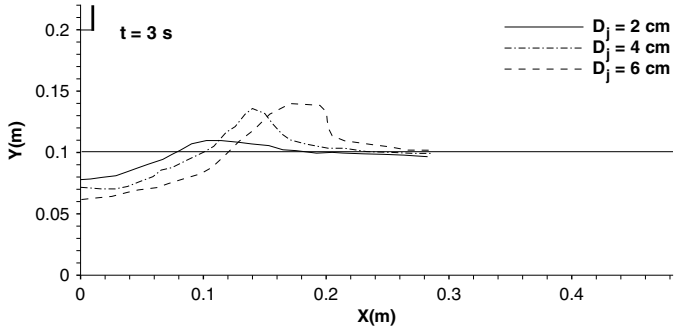

Fig. 18. Crater profiles under different nozzle widths D_j, in the case of $V_j = 1$ m/s and $H_j = 0.1$ m.

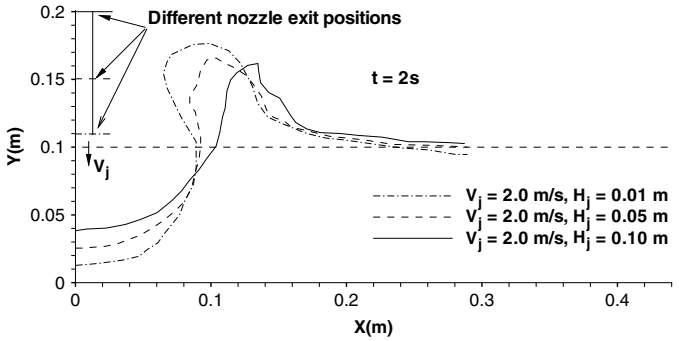

Fig. 19. Crater profiles under different impinging heights H_j, in the case of $D_j = 0.02$ m.

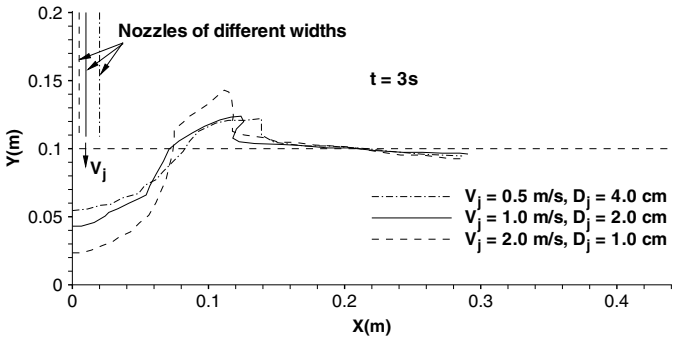

Fig. 20. Crater profiles under constant jet flux Q and fixed impinging height $H_j = 1$ cm.

the proposed SPH model if the geometrical length scale of the studied problem is large enough, as illustrated in the previous wall jet scour case. However, this would result in a huge increase of the computational costs. In fact, in the current study, due to the explicit time-stepping algorithm used in the model, the applicable range of jetting velocity is dependent on the Courant-Friedrich-Levy (CFL) condition

$$\Delta t \leq C_{\text{cour}} \min(h/c_s, h/c_f) \tag{31}$$

where C_{cour} = Courant coefficient; h = smoothing length of particles; and c_s and c_f = virtual sound speed of solid and water, respectively. If large jetting velocity is used, small time step size or large particle spacing should be employed. This is already illustrated in the wall jet scouring case. In the current impinging jet excavation model, the dimensions of the rectangular tank and the particle number in it were fixed. In order to simulate high-velocity water jet excavation, a very small time step size should be used. If the total time steps are constant, we can get only a very short time simulation of the excavation process.

Fig. 18 shows the crater profiles at a certain instant $t = 3$ s with different nozzle widths D_j. As expected, the crater size increases with the increase of nozzle width, especially the crater width. Thus, for some excavation operations, such as trenching in pipeline engineering, a wide nozzle can be used to obtain a wide trench for large pipelines.

Aderibigbe and Rajaratnam (1996) studied the erosion of loose beds of sand by submerged circular impinging vertical turbulent jets. They revealed two major flow regimes referred to as the strongly deflected (SD) and the weakly deflected (WD) jet regimes. In Moore and Masch (1962), two types of scour holes, one being wide and shallow and the other being deep and narrow, were also found to exist. The conditions of their occurrence were established according to the height of the nozzle exit above the soil surface, i.e., the impinging height H_j in this paper. This effect was also investigated in the current numerical simulation. Fig. 19 gives the crater profiles under different impinging heights H_j. It is seen that the crater depth increased with the decrease of the impinging height. Especially, the crater profile made a big difference with the impinging heights. For a very small impinging height, the crater profile exhibited a headstand Ω-shape, while a shallow U-shape was formed for larger impinging height. This is reasonable because for the lower H_j values, the potential core of the water jet struck directly on the soil surface and the jet was almost completely reversed. For the higher H_j values, the potential core of the jet did not strike the sample and the jet was of broader extent, causing a relatively wide and shallow scour hole.

In practical engineering, a question about the efficiency of the jetting operation is which choice, with the same jet flux $Q = D_j V_j$, either using lower V_j with larger D_j or using higher V_j with smaller D_j, is more efficient in terms of crater depth. Fig. 20 answers this question. It is seen that with a smaller nozzle but a higher jetting velocity, the crater is deeper. However, the width is almost the same. Thus, in order to obtain a deeper crater, a smaller nozzle with a higher jetting velocity is recommended.

Effects of Cohesion and Dilatancy

Having considered the effects of the nozzle, now we investigated the effects of soil parameters. In Wang et al. (2016a), the effects of internal friction angle and hydraulic conductivity on the excavation profiles were investigated. In the current study, however, some other factors that may also contribute to the formation of the different profiles were found. For example, cohesion of soil is also a factor affecting the excavation process. The effect of cohesion on scour has been discussed by Ansari et al. (2003), Mazurek et al. (2003), and Mazurek and Hossain (2007). Mazurek and Hossain (2007) found that excavation in cohesionless and cohesive soils varies appreciably, which makes developing a unified method to predict scour by impinging jets more difficult. In the present study, however, effects of cohesion on the excavation can be easily taken into account. Granular materials, such as sand or glass beads, are cohesionless, while some hard clay can have a cohesion in magnitude of tens of kilopascals. Fig. 21 shows the crater profiles formed in both cohesive and cohesionless soils, respectively. Cohesion ranging from 50 Pa to 25 kPa was investigated. It is seen that in a cohesive soil, a smaller excavation was obtained due to the higher strength of this kind of soil. Excavation would be difficult in a hard clay with 25-kPa cohesive force.

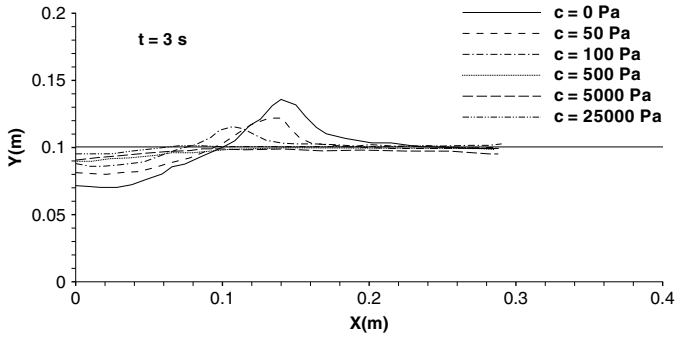

Fig. 21. Cohesion effects on the excavation ($V_j = 1.0$ m/s, $D_j = 0.02$ m, and $H_j = 0.1$ m).

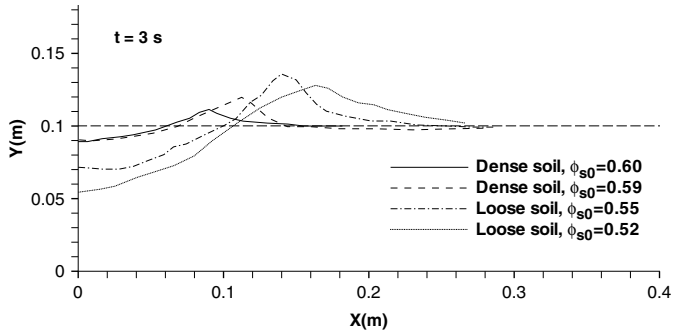

Fig. 22. Excavation of soils with different initial packing states, in the case of $D_j = 0.04$ m, $V_j = 1$ m/s, and $H_j = 0.1$ m.

In addition, it was found that dilatancy or compaction of soil can have prominent effects on the excavation profile. According to the theory of critical state, loose packing material exhibits compaction when subjected to large deformation. As a result of the compaction, the interstitial pore water is squeezed out from the soil, increasing the pore-water pressure or equivalently decreasing the efficient pressure acting on the solid skeleton, which in turn decreases the Coulomb friction between solid particles and thereby enhances the mobility of the soil. On the contrary, dense soil undergoes dilatancy, which increases the friction and decreases the mobility of the soil. Effects of dilatancy or compaction on the submerged water jet soil excavation are illustrated in Fig. 22. It is shown that dilatancy or compaction had a great influence on the shape of the excavation hole. When the mixture was initially dense packed, the excavation hole was shallow and narrow. Increase of the water content improved the soil mobility. This conclusion is generally consistent with that of Nguyen et al. (2017) where the influence of water content on the erosion parameters of a silty soil was investigated using an improved jet erosion test device. Specially, in Nguyen et al. (2017), a Proctor optimum value of the water content was reported due to the fabric of the soil, which depends highly on the permeability or infiltration of the pore water. In the current study, the permeability (i.e., the hydraulic conductivity) was constant, thus the coupled effects of the water content and soil permeability on the excavation were not investigated here.

Fig. 23 shows the pore water pressure field at the initial static state and $t = 1$ s, respectively. According to the theory of critical state, dense packing material exhibits dilation subject to a shear. As a result of the dilation, the interstitial pore water is sucked in from the ambient water, giving rise to a negative excess pore pressure field. Here, negative means the pressure is lower than the hydrostatic pressure of the surrounding fluid at the same depth, as shown in Fig. 23. This pore water feedback mechanism explains the dilatancy effects on dense granular saturated mixture flows.

Conclusions

In this paper, submerged soil excavation by high-velocity water jet was investigated by means of a two-fluid smoothed-particle hydrodynamics method. A critical state theory was coupled to account for the dilatancy or compaction effects of the soil on the excavation performance. A reinitialization technique was developed in the SPH approach to retain the abrupt change of the water volume fraction at the interface of the granular material and the surrounding fluid. An alternative treatment of the pressure term in the momentum equation for fluid also helped to reduce the numerical instability in the calculation of fluid phase. Some special treatments of inflow and overflow conditions, as well as improvements to avoid unphysical voids in flow fields, were presented.

Numerical simulations for excavations by plane wall jet and vertical impinging jet were presented. The numerical results agreed well with other researchers' numerical and experimental results. The effects of the nozzle width, impinging height, jetting velocity, and water flux on the formation of different crater patterns were examined. Soil parameters, such as cohesion and dilatancy, were also studied. Cohesions in the range of 50 Pa to 25 kPa were applicable in the proposed SPH model. The jetting velocities V_j less than 5 m/s were illustrated in the simulation, although higher jetting

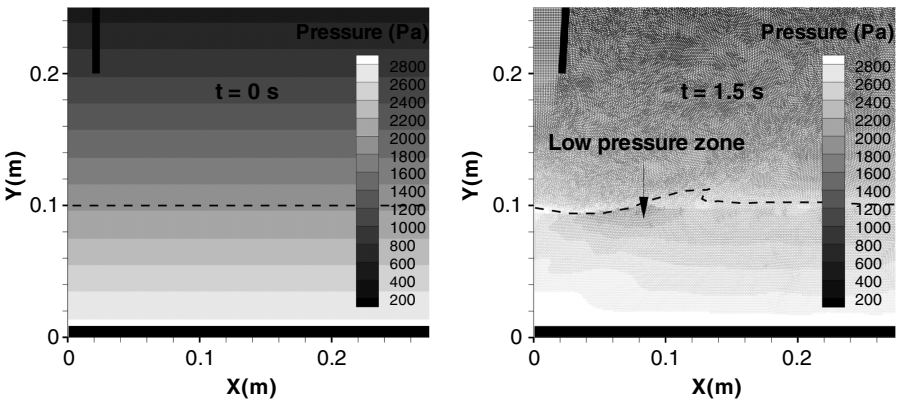

Fig. 23. Water pressure fields at the initial stage of the dense soil excavation ($D_j = 0.04$ m, $V_j = 1$ m/s, $H_j = 0.1$ m, and $\phi_{s0} = 0.60$).

velocities are also applicable if large geometric models are considered. Computational results illustrated the critical role of dilatancy in linking coevolution of the solid volume fraction and pore fluid pressure, by modifying the Coulomb friction, and thereby regulating the dynamics of soil deformation. The proposed method is robust and efficient, and can be applied to water-soil mixture flows in subsea engineering and geomechanics.

Although short-term simulations show good agreement with other researchers' experimental and numerical results, long-term simulations still need to be conducted in the future. Long-term simulation requires developments on fast computing algorithms and the corresponding computer hardware. Recent developments on GPU-based numerical simulation techniques provide us with an approach to solve this problem. Large-scale GPU-based simulation of the excavation process using the proposed two-fluid SPH model will be performed in the future.

In this paper, large deformation and failure of soil under the impingement of high-velocity water jet were investigated, where the soil was considered as an elastoplastic material. However, as mentioned, during the excavation process different regimes of water-granular interaction exist and make dominant contributions at different stages, such as transportation of suspended load and sedimentation. In addition, effects of turbulence of water jet on the excavation were also prominent in the mixture flow. Thus, in order to predict the evolution of the excavation, it is necessary to take all these flow regimes into account. However, these would be topics for the future.

References

Ade, F., and N. Rajaratnam. 1998. "Generalized study of erosion by circular horizontal turbulent jets." *J. Hydraul. Res.* 36 (4): 613–636. https://doi.org/10.1080/00221689809498612.

Aderibigbe, O., and N. Rajaratnam. 1998. "Effect of sediment gradation on erosion by plane turbulent wall jets." *J. Hydraul. Eng.* 124 (10): 1034–1042. https://doi.org/10.1061/(ASCE)0733-9429(1998)124:10(1034).

Aderibigbe, O. O., and N. Rajaratnam. 1996. "Erosion of loose beds by submerged circular impinging vertical turbulent jets." *J. Hydraul. Res.* 34 (1): 19–33. https://doi.org/10.1080/00221689609498762.

Akashi, N., and T. Saito. 1980. "Studies on the scour from submerged impinged jet." [In Japanese.] *Proc. Jpn. Soc. Civ. Eng.* 1980 (298): 53–62. https://doi.org/10.2208/jscej1969.1980.298_53.

Ali, K. H. M., and S. Y. Lim. 1986. "Local scour caused by submerged wall jets." *Proc. Inst. Civ. Eng.* 81 (4): 607–645. https://doi.org/10.1680/iicep.1986.464.

Ali, K. H. M., and A. A. S. Neyshaboury. 1991. "Localized scour downstream of a deeply submerged horizontal jet." *Proc. Inst. Civ. Eng.* 91 (1): 1–18. https://doi.org/10.1680/iicep.1991.13579.

Amicarelli, A., G. Agate, and R. Guandalini. 2013. "A 3D fully Lagrangian smoothed particle hydrodynamics model with both volume and surface discrete elements." *Int. J. Numer. Methods Eng.* 95 (5): 419–450. https://doi.org/10.1002/nme.4514.

Amicarelli, A., B. Kocak, S. Sibilla, and J. Grabe. 2017. "A 3D smoothed particle hydrodynamics model for erosional dam-break floods." *Int. J. Comput. Fluid Dyn.* 31 (10): 413–434. https://doi.org/10.1080/10618562.2017.1422731.

Andreotti, B., Y. Forterre, and O. Pouliquen. 2013. *Granular media: Between fluid and solid*. Cambridge, UK: Cambridge University Press.

Ansari, S. A., U. C. Kothyari, and K. G. R. Raju. 2003. "Influence of cohesion on scour under submerged circular vertical jets." *J. Hydraul. Eng.* 129 (12): 1014–1019. https://doi.org/10.1061/(ASCE)0733-9429(2003)129:12(1014).

Bear, J., and J.-M. Buchlin, eds. 1991. *Modelling and applications of transport phenomena in porous media*. Dordrecht, Netherlands: Springer.

Beltaos, S., and N. Rajaratnam. 1973. "Plane turbulent impinging jets." *J. Hydraul. Res.* 11 (1): 29–59. https://doi.org/10.1080/00221687309499789.

Bui, H. H., R. Fukagawa, K. Sako, and S. Ohno. 2008. "Lagrangian meshfree particles method (SPH) for large deformation and failure flows of geomaterial using elastic-plastic soil constitutive model." *Int. J. Numer. Anal. Methods Geomech.* 32 (12): 1537–1570. https://doi.org/10.1002/nag.688.

Bui, H. H., R. Fukagawa, K. Sako, and J. Wells. 2011. "Slope stability analysis and discontinuous slope failure simulation by elasto-plastic smoothed particle hydrodynamics (SPH)." *Geotechnique* 61 (7): 565–574. https://doi.org/10.1680/geot.9.P.046.

Chatterjee, S. S., S. N. Ghosh, and M. Chatterjee. 1994. "Local scour due to submerged horizontal jet." *J. Hydraul. Eng.* 120 (8): 973–992. https://doi.org/10.1061/(ASCE)0733-9429(1994)120:8(973).

Crespo, A., M. Gómez-Gesteira, and R. A. Dalrymple. 2007. "Boundary conditions generated by dynamic particles in SPH methods." *Comput. Mater. Continua* 5 (3): 173–184.

Ferrand, M., D. R. Laurence, B. D. Rogers, D. Violeau, and C. Kassiotis. 2013. "Unified semi-analytical wall boundary conditions for inviscid, laminar or turbulent flows in the meshless SPH method." *Int. J. Numer. Methods Fluids* 71 (4): 446–472. https://doi.org/10.1002/fld.3666.

Gomez-Gesteira, M., B. Rogers, A. Crespo, R. Dalrymple, M. Narayanaswamy, and J. Dominguez. 2012. "SPHysics: Development of a free-surface fluid solver. Part 1: Theory and formulations." *Comput. Geosci.* 48: 289–299. https://doi.org/10.1016/j.cageo.2012.02.029.

Hettinger, F., and J. Machin. 2005. "Cable and pipeline burial at 3,000 meters." In *Proc., OCEANS 2005 MTS/IEEE*. Piscataway, NJ: IEEE.

Hill, D. F., and B. D. Younkin. 2006. "PIV measurements of flow in and around scour holes." *Exp. Fluids* 41 (2): 295–307. https://doi.org/10.1007/s00348-006-0156-3.

Hogg, A. J., H. E. Huppert, and W. B. Dade. 1997. "Erosion by planar turbulent wall jets." *J. Fluid Mech.* 338: 317–340. https://doi.org/10.1017/S0022112097005077.

Ikari, H., H. Gotoh, T. Tanbo, and T. Ejiri. 2015. "MPS-based simulation of scouring due to submerged vertical jet with sub-particle-scale suspended load model." [In Japanese.] *J. Jpn. Soc. Civ. Eng. B2* 71 (2): I_19–I_24.

Iverson, R. M. 2000. "Landslide triggering by rain infiltration." *Water Resour. Res.* 36 (7): 1897–1910. https://doi.org/10.1029/2000WR900090.

Iverson, R. M. 2005. "Regulation of landslide motion by dilatancy and pore pressure feedback." *J. Geophys. Res.* 110 (F2): F02015. https://doi.org/10.1029/2004JF000268.

Jackson, R. 2000. *The dynamics of fluidized particles*. Cambridge, UK: Cambridge University Press.

Libersky, L., and A. Petschek. 1991. "Smooth particle hydrodynamics with strength of materials." In Vol. 395 of *Advances in the free-Lagrange method including contributions on adaptive gridding and the smooth particle hydrodynamics method*, edited by H. Trease, M. Fritts, and W. Crowley, 248–257. Berlin: Springer.

Lind, S., R. Xu, P. Stansby, and B. Rogers. 2012. "Incompressible smoothed particle hydrodynamics for free-surface flows: A generalised diffusion-based algorithm for stability and validations for impulsive flows and propagating waves." *J. Comput. Phys.* 231 (4): 1499–1523. https://doi.org/10.1016/j.jcp.2011.10.027.

Machin, J. B., and P. A. Allan. 2011. "State-of-the-art jet trenching analysis in stiff clays." In *Proc., 2nd Int. Symp. on Frontiers in Offshore Geotechnics*. London: Taylor & Francis.

Machin, J. B., F. D. Messina, J. K. Mangal, J. Girard, and M. Finch. 2001. "Recent research on stiff clay jetting." In *Proc., Offshore Technology Conf.*, OTC-13139. Houston: Perry Slingsby Systems.

Manenti, S., S. Sibilla, M. Gallati, G. Agate, and R. Guandalini. 2012. "SPH simulation of sediment flushing induced by a rapid water flow." *J. Hydraul. Eng.* 138 (3): 272–284. https://doi.org/10.1061/(ASCE)HY.1943-7900.0000516.

Mazurek, K. A., and T. Hossain. 2007. "Scour by jets in cohesionless and cohesive soils." *Can. J. Civ. Eng.* 34 (6): 744–751. https://doi.org/10.1139/l07-005.

Mazurek, K. A., and N. Rajaratnam. 2005. "Erosion of sand beds by obliquely impinging plane turbulent air jets." *J. Hydraul. Res.* 43 (5): 567–573. https://doi.org/10.1080/00221680509500155.

Mazurek, K. A., N. Rajaratnam, and D. C. Sego. 2001. "Scour of cohesive soil by submerged circular turbulent impinging jets." *J. Hydraul. Eng.* 127 (7): 598–606. https://doi.org/10.1061/(ASCE)0733-9429(2001)127:7(598).

Mazurek, K. A., N. Rajaratnam, and D. C. Sego. 2003. "Scour of a cohesive soil by submerged plane turbulent wall jets." *J. Hydraul. Res.* 41 (2): 195–206. https://doi.org/10.1080/00221680309499961.

Monaco, A. D., S. Manenti, M. Gallati, S. Sibilla, G. Agate, and R. Guandalini. 2011. "SPH modeling of solid boundaries through a semi-analytic approach." *Eng. Appl. Comput. Fluid Mech.* 5 (1): 1–15. https://doi.org/10.1080/19942060.2011.11015348.

Monaghan, J. J. 1994. "Simulating free surface flows with SPH." *J. Comput. Phys.* 110 (2): 399–406. https://doi.org/10.1006/jcph.1994.1034.

Moore, W. L., and F. D. Masch. 1962. "Experiments on the scour resistance of cohesive sediments." *J. Geophys. Res.* 67 (4): 1437–1446. https://doi.org/10.1029/JZ067i004p01437.

Morris, J. P., P. J. Fox, and Y. Zhu. 1997. "Modeling low Reynolds number incompressible flows using SPH." *J. Comput. Phys.* 136 (1): 214–226. https://doi.org/10.1006/jcph.1997.5776.

Nguyen, V.-N., J.-R. Courivaud, P. Pinettes, H. Souli, and J.-M. Fleureau. 2017. "Using an improved jet-erosion test to study the influence of soil parameters on the erosion of a silty soil." *J. Hydraul. Eng.* 143 (8): 04017018. https://doi.org/10.1061/(ASCE)HY.1943-7900.0001305.

Pailha, M., M. Nicolas, and O. Pouliquen. 2008. "Initiation of underwater granular avalanches: Influence of the initial volume fraction." *Phys. Fluids* 20 (11): 111701. https://doi.org/10.1063/1.3013896.

Pailha, M., and O. Pouliquen. 2009. "A two-phase flow description of the initiation of underwater granular avalanches." *J. Fluid Mech.* 633: 115–135. https://doi.org/10.1017/S0022112009007460.

Perng, A. T. H., and H. Capart. 2008. "Underwater sand bed erosion and internal jump formation by travelling plane jets." *J. Fluid Mech.* 595: 1–43. https://doi.org/10.1017/S0022112007008567.

Rajaratnam, N. 1981. "Erosion by plane turbulent jets." *J. Hydraul. Res.* 19 (4): 339–358. https://doi.org/10.1080/00221688109499508.

Rajaratnam, N., and K. A. Mazurek. 2003. "Erosion of sand by circular impinging water jets with small tailwater." *J. Hydraul. Eng.* 129 (3): 225–229. https://doi.org/10.1061/(ASCE)0733-9429(2003)129:3(225).

Schaeffer, D. G. 1987. "Instability in the evolution equations describing incompressible granular flow." *J. Differ. Equation* 66 (1): 19–50. https://doi.org/10.1016/0022-0396(87)90038-6.

Shadloo, M. S., A. Zainali, M. Yildiz, and A. Suleman. 2012. "A robust weakly compressible SPH method and its comparison with an incompressible SPH." *Int. J. Numer. Methods Eng.* 89 (8): 939–956. https://doi.org/10.1002/nme.3267.

Ulrich, C., M. Leonardi, and T. Rung. 2013. "Multi-physics SPH simulation of complex marine-engineering hydrodynamic problems." *Ocean Eng.* 64: 109–121. https://doi.org/10.1016/j.oceaneng.2013.02.007.

Vacondio, R., B. Rogers, P. Stansby, P. Mignosa, and J. Feldman. 2013. "Variable resolution for SPH: A dynamic particle coalescing and splitting scheme." *Comput. Methods Appl. Mech. Eng.* 256: 132–148. https://doi.org/10.1016/j.cma.2012.12.014.

Wang, C., Y. Wang, C. Peng, and X. Meng. 2016a. "Smoothed particle hydrodynamics simulation of water-soil mixture flows." *J. Hydraul. Eng.* 142 (10): 04016032. https://doi.org/10.1061/(ASCE)HY.1943-7900.0001163.

Wang, C., Y. Wang, C. Peng, and X. Meng. 2017a. "Dilatancy and compaction effects on the submerged granular column collapse." *Phys. Fluids* 29 (10): 103307. https://doi.org/10.1063/1.4986502.

Wang, C., Y. Wang, C. Peng, and X. Meng. 2017b. "Two-fluid smoothed particle hydrodynamics simulation of submerged granular column collapse." *Mech. Res. Commun.* 79: 15–23. https://doi.org/10.1016/j.mechrescom.2016.12.001.

Wang, D., S. Li, T. Arikawa, and H. Gen. 2016b. "ISPH simulation of scour behind seawall due to continuous tsunami overflow." *Coastal Eng. J.* 58 (3): 1650014. https://doi.org/10.1142/S0578563416500145.

Wang, D., S. Shao, S. Li, Y. Shi, T. Arikawa, and H. Zhang. 2018. "3D ISPH erosion model for flow passing a vertical cylinder." *J. Fluids Struct.* 78: 374–399. https://doi.org/10.1016/j.jfluidstructs.2018.01.003.

Xu, R., P. Stansby, and D. Laurence. 2009. "Accuracy and stability in incompressible SPH (ISPH) based on the projection method and a new approach." *J. Comput. Phys.* 228 (18): 6703–6725. https://doi.org/10.1016/j.jcp.2009.05.032.

Yeh, P.-H., K.-A. Chang, J. Henriksen, B. Edge, P. Chang, A. Silver, and A. Vargas. 2009. "Large-scale laboratory experiment on erosion of sand beds by moving circular vertical jets." *Ocean Eng.* 36 (3–4): 248–255. https://doi.org/10.1016/j.oceaneng.2008.11.006.

Yuan, Q., M. Zhao, C. Wang, and T. Ge. 2018. "Numerical study of sand scour with a modified Eulerian model based on incipient motion theory." *Mar. Georesour. Geotechnol.* 36 (7): 818–826. https://doi.org/10.1080/1064119X.2017.1390710.

Zhang, S., C. Wang, and T. Ge. 2017. "Experimental prediction of the noncontact jet trencher's excavation depth in clay." *Mar. Georesour. Geotechnol.* 35 (2): 300–304. https://doi.org/10.1080/1064119X.2016.1149530.

Zhang, S., M. Zhao, T. Ge, and C. Wang. 2016. "Experimental research on trenching in stiff clay by submerged vertical traveling jets." *J. Coastal Res.* 32 (2): 365–373. https://doi.org/10.2112/JCOASTRES-D-14-00038.1.